

Gradient Descent in Materio

Marcus N. Boon^{1*}, Hans-Christian Ruiz Euler¹, Tao Chen¹, Bram van de Ven¹, Unai Alegre Ibarra¹, Peter A. Bobbert^{1,2}, Wilfred G. van der Wiel^{1†}

¹NanoElectronics Group, MESA+ Institute for Nanotechnology and BRAINS Center for Brain-Inspired Nano Systems, University of Twente, PO Box 217, Enschede 7500 AE, The Netherlands.

²Molecular Materials and Nanosystems & Center for Computational Energy Research, Department of Applied Physics, Eindhoven University of Technology, PO Box 513, Eindhoven 5600 MB, The Netherlands.

*Current address: Modelling of Cognitive Processes, Department for Electrical Engineering and Computer Science, Technische Universität Berlin

†Correspondence to: W.G.vanderWiel@utwente.nl

Summary paragraph

Deep learning, a multi-layered neural network approach inspired by the brain, has revolutionized machine learning¹. One of its key enablers has been backpropagation², an algorithm that computes the gradient of a loss function with respect to the weights in the neural network model, in combination with its use in gradient descent^{3,4}. However, the implementation of deep learning in digital computers is intrinsically wasteful, with energy consumption becoming prohibitively high for many applications⁵. This has stimulated the development of specialized hardware, ranging from neuromorphic CMOS integrated circuits⁶⁻⁸ and integrated photonic tensor cores⁹ to unconventional, material-based computing systems¹⁰⁻¹⁵. The learning process in these material systems, taking place, e.g., by artificial evolution^{14,15} or surrogate neural network modelling¹⁶, is still a complicated and time-consuming process. Here, we demonstrate an efficient and accurate homodyne gradient extraction method for performing gradient descent on the loss function directly in the material system. We demonstrate the method in our recently developed dopant network processing units¹⁶, where we readily realize all Boolean gates. This shows that gradient descent can in principle be fully implemented *in materio* using simple electronics, opening up the way to autonomously learning material systems.

Main text:

For tuneable complex systems parameter optimization is a crucial task, which becomes increasingly time consuming as the dimensionality of the parameter space increases. Some optimization methods are tailored to certain systems. For example, in deep learning¹, the input-output relation of a deep neural network (DNN) model is given by a differentiable, multi-variable function, where gradient information can be readily obtained from the (partial) derivatives. Backpropagation² is used to efficiently compute the gradient of a pre-defined loss function with respect to the DNN parameters (weights and biases), which allows for training complex DNN models consisting of thousands to millions of parameters. Iterative, gradient-based optimization methods, such as stochastic gradient descent^{3,4}, are already optimized for speed and accuracy.

In contrast, for many physical systems no *a priori* analytical description of their behaviour is known, and an *in situ* gradient-based optimization method of their behaviour is therefore not directly available. Instead, tuning is often done by hand or with the assistance of an external computer. For example, for tuning quantum devices, grid scanning techniques and scan processing were proposed using search heuristics^{17–19} or machine-learning^{20–24}. Other approaches learn the system response, and obtain gradient information by linear statistical methods²⁵, or, as we recently showed, by modelling the entire system with a DNN, optimizing the DNN using gradient descent, and transferring the optimized DNN parameters to the physical device¹⁶. While accelerating the procedure, such optimization is complicated and case-specific, preventing autonomous operation. Particularly for the application of brain-inspired devices^{10–12,26,27} in edge computing^{14,15,28,29} this is problematic, as dependence on external systems is undesired³⁰.

Here, we demonstrate an efficient, on-chip gradient extraction method for gradient-based optimization of complex (*viz.* multi-terminal, non-linear) nanoelectronic devices, which we call *homodyne gradient extraction* (HGE). Existing gradient-based methods, using finite differences to estimate the gradient locally, such as ‘weight perturbation’³¹, require many measurements per iteration. For each additional parameter to be optimized, at least two additional measurements are needed to approximate the gradient with respect to that parameter, which limits scalability. Whereas finite-difference methods perturb only one parameter at a time, requiring at least $2p$ measurements for a p -dimensional parameter space, simultaneous perturbation methods^{32,33} perturb all parameters at the same time with random magnitude, requiring only two measurements per iteration. However, since the search direction is random, such methods do not exactly follow the gradient

path, and therefore require on average more iterations to converge. Next to scalability, maintaining the quality of the gradient approximation is another requirement, which can be challenging due to the system's inherent noise. Our alternative HGE method estimates the gradient components both accurately and in parallel. It involves perturbation of all parameters simultaneously, but at the same time recovers the gradient components in each dimension separately. The method requires only a short measurement time per iteration to determine all gradient components. Moreover, our method can in principle be fully realized in electronics, *i.e.* without signal processing on a digital computer, enabling the realization of fully autonomously optimizing systems.

General concept

The general concept of our HGE optimization method is presented schematically in Fig. 1 for a nanoelectronic device with, as an example, N voltage inputs and one current output, I_{out} . Before initializing the optimization process, a loss function $E(\mathbf{V})$ is defined (with \mathbf{V} a vector of all optimizable voltages), which expresses the proximity of the actual output to a desired output. This function by definition depends on I_{out} , which in turn depends on the voltage inputs \mathbf{V} . By using the chain rule, the derivative of the loss function E with respect to each optimizable parameter is factored into the derivative of the loss function with respect to the output, dE/dI_{out} , and the derivatives of the output with respect to each optimizable parameter, gathered in the gradient $\nabla I_{\text{out}}(\mathbf{V})$. The essence of our HGE method is that $\nabla I_{\text{out}}(\mathbf{V})$ does not need to be calculated using an analytical description of the system, but that it can be straightforwardly derived from its input-output relations. In HGE (see Fig. 1), small sinusoidal voltage perturbations $v_i(t) = \alpha_i \sin(2\pi f_i t)$ are added to all optimizable DC voltages V_i *in parallel*, where each perturbation has a distinct frequency f_i and optionally a distinct amplitude α_i , after which the corresponding changes $i_i(t)$ in I_{out} are recovered. By using distinct frequencies, we exploit the orthogonality of sinusoidal functions in the space of all possible time-dependent functions and a principle similar to lock-in (or homodyne) detection. I_{out} is multiplied (in a digital computer for now, but straightforwardly realizable in electronics) by in-phase and 90 degrees phase-shifted (quadrature) sinusoidal signals with the same frequencies f_1, f_2, \dots, f_N as the input signal perturbations. For each frequency f_i , the two resulting components (X_i and Y_i in Fig. 1) are used to determine the magnitude $A_i = \sqrt{X_i^2 + Y_i^2}$ of the output signal corresponding to this input frequency (see Methods for details). These values A_1, A_2, \dots, A_N are

proportional to the changes in I_{out} due to the sinusoidal perturbations on inputs 1 to N . To approximate the partial derivatives of I_{out} with respect to each input voltage, $\partial I_{\text{out}}(\mathbf{V}) / \partial V_i$, the amplitudes $[A_1, \dots, A_N]$ are divided by the amplitudes α_i . Next, the derivative of the loss function with respect to the output current, dE/dI_{out} , is computed and multiplied with $\nabla I_{\text{out}}(\mathbf{V})$ to obtain the gradient of the loss function with respect to the input voltages V_i . Finally, the input voltages are updated by means of an iterative optimization scheme. A simple first-order optimization scheme is used with a learning rate η , as shown in Fig. 1. This process is repeated until a maximum number of iterations is reached, or an early stopping criterium is met, in this case a threshold value for the loss function. Here, $\nabla I_{\text{out}}(\mathbf{V})$ is calculated in a digital computer (see Methods), but its evaluation can be easily implemented electronically in a way usual in (multi-channel) lock-in amplifiers. The averaging of the signals that results from multiplying I_{out} and the reference signal to obtain the vectors \mathbf{X} and \mathbf{Y} can be realized by a low-pass filter instead. Furthermore, depending on the loss function, taking the derivative with respect to the output current, dE/dI_{out} , can also be directly implemented in electronics. Detailed guidelines on picking the perturbation frequencies can be found in Methods.

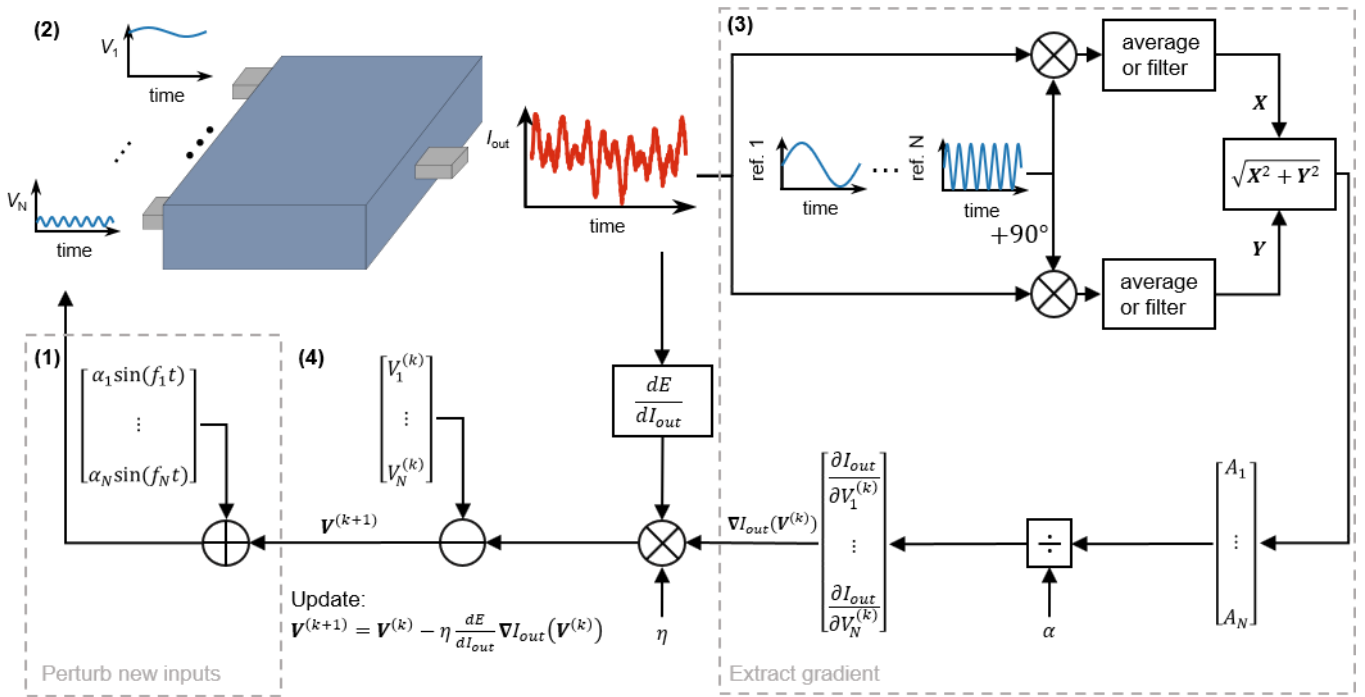


Figure 1 | Gradient descent in materio using homodyne gradient extraction (HGE). (1) Small sinusoidal voltage signals (with distinct frequencies $[f_1, \dots, f_N]$ and amplitudes $[\alpha_1, \dots, \alpha_N]$) are added to the DC voltage inputs. (2) The output current I_{out} (red curve) is affected by each distinct input sine wave. (3) The magnitude of I_{out} for each frequency used in the input voltages is recovered by using the principles of lock-in (homodyne) detection. These magnitudes (vector \mathbf{A}) are divided by the amplitudes of the input sine waves (vector $\boldsymbol{\alpha}$) of the corresponding frequencies, extracting the derivatives of the output current with respect to

each input voltage, $[\partial I_{out}/\partial V_1^{(k)}, \dots, \partial I_{out}/\partial V_N^{(k)}]$. (4) The approximated gradient is multiplied by the derivative of the loss function with respect to the output current, dE/dI_{out} , and by the learning parameter η , and is used to update the input voltages in an iterative manner.

We experimentally demonstrate this approach in a brain-inspired, nanoelectronic multi-terminal device, which we refer to as doping network processing unit (DNPU)^{15,16,34}. The device consists of an electrically tuneable network of arsenic dopants in silicon (Si:As) with eight terminals, seven of which act as voltage inputs and one as current output (see Supplementary Note 1 and Extended Data Figures 1-4 for the results on a boron dopant network (Si:B) device). We have previously shown that the Si:B devices can be tuned to solve linearly inseparable classification problems³⁵. This was done using an evolutionary approach^{14,15,29}, or with gradient descent on a DNN model of the physical device¹⁶. In the present work we will demonstrate the use of HGE to realize functionality.

To validate our approach, we compare the HGE gradients with those calculated in a DNN model of one of our devices. The DNN model provides the advantage that the gradients can be obtained analytically with backpropagation¹⁶, allowing us to verify that the HGE gradients can in principle closely match the analytical gradients. After this validation, we switch to a physical device for the remainder of the paper and demonstrate that the accuracy of HGE increases for increasing sampling time. Furthermore, we show that the homodyne extraction of the derivative of the output current with respect to a given input voltage is not affected by the sinusoidal perturbations of other input voltages, by comparing the extracted derivatives when perturbing only a single input voltage to the extracted derivatives when perturbing all input voltages simultaneously. This means that the perturbations can be taken large enough to exceed the noise, but small enough to be in the linear response regime of the device. Hence, all input voltages can be perturbed simultaneously, substantiating the scalability of our approach. Finally, we use gradient descent *in materio* to realize all Boolean logic gates, and compare the results to earlier approaches^{15,16}.

HGE validation in a DNN surrogate model

Figure 2 shows a validation of HGE using a DNN surrogate model of the device. First, we train a DNN to represent the input-output relations of the physical device (see Ref. 16 for details). A schematic representation

of the surrogate DNN model is shown in Fig. 2a, illustrating the two methods for computing the gradients in the DNN model. (1) The orange arrows show how gradients are normally computed in DNNs. By performing a forward pass (*viz.* inserting input values $[V_1, \dots, V_7]$ in the DNN and computing the output value I_{out}) and a backward pass via backpropagation, the gradient information is retrieved. Note that we perform this gradient calculation on the voltage inputs rather than on the internal weights of the DNN, as we here use a DNN that is already trained to represent a given physical device. The internal weights therefore remain frozen. (2) The blue arrows show how the gradients are estimated with HGE. The voltage inputs of the DNN are sinusoidally perturbed with distinct frequencies and the gradients are obtained as explained in Fig. 1.

Figure 2b shows the derivatives (gradient components) of the output current with respect to any of the 7 input voltages as red dots. We randomly and uniformly sampled 3,000 points from an input range of $[-1, 1]$ V and computed the gradient both with backpropagation and HGE. The x -coordinate is the analytical derivative computed by backpropagation and the y -coordinate is the HGE derivative, both calculated within the DNN model. Ideally, these values match and lie on the black identity line. Several effects could lead to errors in the HGE. First, the contribution from any signal that is not at the same frequency as the reference signal is not fully averaged to zero because of the finite measurement time (see Methods for details). Second, for too large input voltage perturbations, the response in the output current will no longer be linear. These issues can be resolved by increasing the sampling time and/or reducing the voltage perturbations. For the HGE parameters used here (see Methods for details), the latter effect contributes most to the error in the gradient. Reducing the voltage perturbations would thus yield better results. However, we aimed to closely match the physical measurements in the next section and therefore used the same parameters in the DNN model. In the physical device, noise masks the response to the sinusoidal perturbations, and therefore the perturbations must be large enough to yield detectable changes in the output current. The HGE derivatives nonetheless closely match the analytical derivatives. We note that the errors in the HGE derivatives are not biased, as shown by the symmetric histogram of the difference between the analytical and HGE derivatives in Fig. 2c.

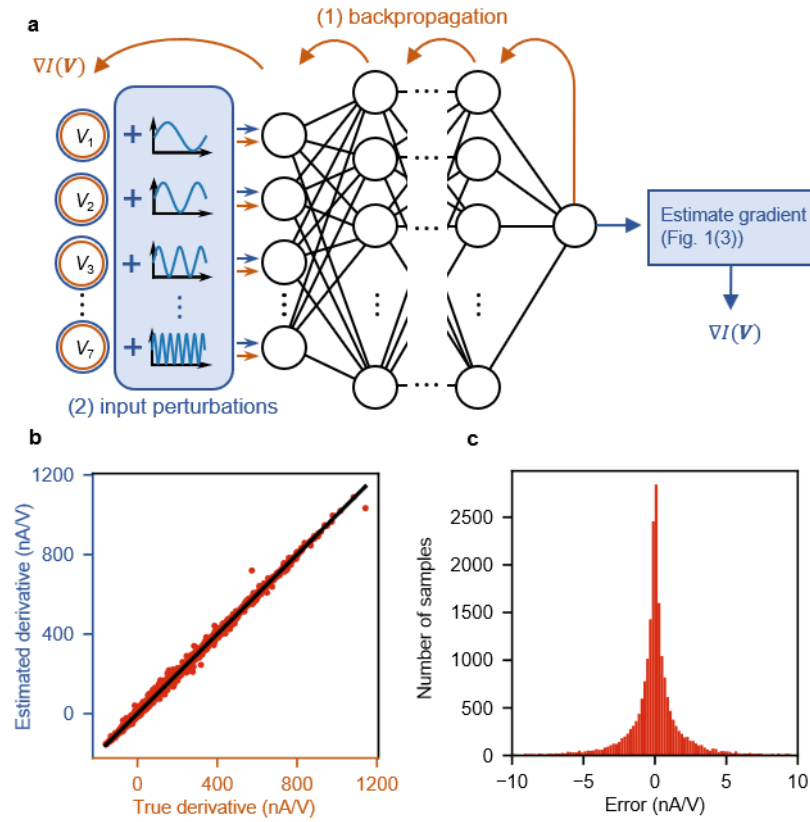


Figure 2 | HGE in a DNN device model. **a**, Demonstration of the two different methods to compute the gradients $\nabla I(\mathbf{V})$. (1) In DNNs gradients are usually computed by performing a forward pass (inserting inputs $[V_1, \dots, V_7]$ in the DNN to compute the output $I(\mathbf{V})$) and a backward pass via backpropagation, as shown by the orange arrows. Since we are interested in the gradient with respect to the inputs, the signal is backpropagated all the way back to the input voltages $[V_1, \dots, V_7]$, while keeping the internal weights fixed. (2) In HGE, indicated by the blue arrows, small perturbations are added to the input voltages and the gradients are extracted as explained in Fig. 1. **b**, Direct comparison between the analytical derivatives, computed with backpropagation, and the HGE derivatives. The solid line has unity slope. **c**, Histogram of the difference in the derivatives computed with the two methods.

HGE *in materio*

We now switch to demonstrating HGE in a physical device, *i.e.* HGE *in materio*. A schematic representation of the physical nanoelectronic device is shown in Fig. 3a. To demonstrate the convergence of the extracted gradients and to determine the sampling time required to obtain accurate results, increasing sampling times are studied. A random DC voltage is applied to each input terminal, and each voltage is perturbed (see Fig. 3a, blue inputs (2)). Figures 3b and c show the extracted derivatives for input terminals 1 and 6, respectively, demonstrating their convergence after only a few cycles of sampling (Extended Data Fig. 5a shows results for all terminals). We obtain sufficient accuracy by setting the sampling time to 10 cycles of the lowest frequency

for the remainder of the experiments. We furthermore investigate how the magnitude of the perturbations influences the accuracy of the extracted gradient. To determine the optimal amplitudes for the sinusoidal perturbations, the accuracy using different sets of increasing amplitudes is tested. Figures 3d and e show the extracted derivatives for input terminals 1 and 6, respectively (Extended Data Fig. 5b and Table 1 give results for all terminals and voltages). The coloured data show the extracted derivatives when applying perturbations to all electrodes simultaneously (*i.e.* inputs (2) in Fig. 3a). These are compared to measurements where derivatives are extracted when perturbing only a single terminal, performing separate measurements to determine each derivative sequentially (*e.g.* for terminal 1, inputs (1) in Fig. 3a), which are indicated by the black solid lines. Since for the latter measurements only one input voltage is perturbed, there cannot be any interference with other input voltages. We conclude that applying multiple input perturbations simultaneously does not cause interference for the used perturbation amplitudes, and thus the extraction of the derivative for an input is independent of the other inputs, which is important for the scaling of the approach. Furthermore, for too small perturbations, the low signal-to-noise ratio prevents an accurate extraction of the gradient. We note that the smallest required perturbation amplitude depends on sampling time: increasing the sampling time allows for smaller perturbations without losing accuracy (see Methods for details). An upper boundary for the amplitude of the perturbations is determined by taking the lowest magnitude that still yields accurate gradients in a noisy environment. Using a larger amplitude than strictly required might introduce errors due to non-linearities in the system response.

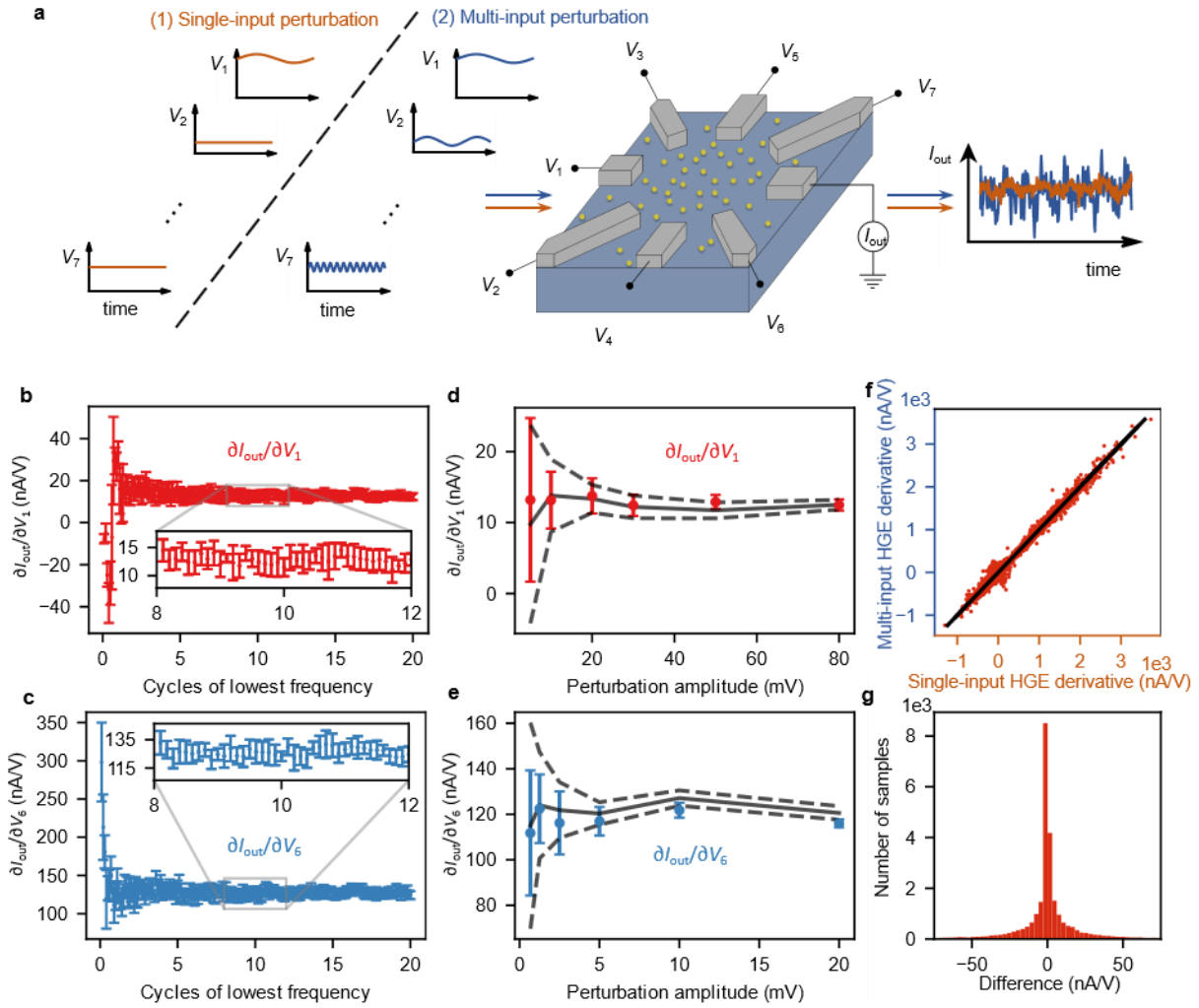


Figure 3 | HGE in a nanoelectronic device. **a**, Schematic representation of the nanoelectronic device (yellow dots represent As atoms) and the different methods to extract the gradient of the output current with respect to the input voltages: single-input (1) and multi-input (2) HGE, compared in d-g. **b**, **c**, Multi-input HGE derivatives for inputs 1 and 6, respectively, as function of time, expressed in cycles of the lowest frequency. The inputs 1 - 7 are biased with a random DC voltage in the range [-1.2, 0.9] V and sinusoidal perturbations with frequencies [20, 50, 30, 90, 130, 190, 230] Hz and amplitudes [30, 20, 20, 10, 10, 5, 5] mV. Since electrodes further away from the output electrode have a smaller influence on the output current, their perturbation amplitudes are chosen higher than those of the electrodes directly neighbouring the output. The longest sampling time is 1 second, corresponding to 20 oscillation cycles of the lowest frequency. **d**, **e**, Extracted derivatives for inputs 1 and 6, respectively, as function of perturbation amplitude. Symbols with error bars: multi-input HGE with 0.5 s measurement time (10 cycles of lowest frequency). Full lines with errors given by dashed lines: single-input HGE with 0.5 s measurement time. The errors represent standard deviations of 10 measurements. **f**, Comparison between the single- and multi-input HGE derivatives for 3,308 random input voltages in the range [-1.2, 0.9] V. The perturbation frequencies are 4 times higher than for the results in b-e, i.e. [80, 200, 120, 360, 520, 760, 920] Hz. The solid line has unity slope. **g**, Histogram of the difference in the single- and multi-input HGE derivatives for the data in f.

Next, we demonstrate the robustness of HGE by comparing multi-input HGE to single-input HGE. This comparison is made for 3,308 random input voltages, using 4 times higher perturbation frequency than above (see Supplementary Note 2 and Extended Data Fig. 6 and 7 for evidence that the gradient estimation is insensitive to the choice of perturbation frequencies). Figures 3f and g show a scatter plot of the multi-input vs the single-input HGE derivatives for all the inputs and a histogram of the differences, respectively. The solid line in Fig. 3f has unity slope. As is visible in Fig. 3g, the histogram is centred around 0 and nearly symmetric. The tails of the difference distribution are more pronounced than in the DNN model (Fig. 2c, note the different x -axis scales) because of the noise present in the experiments, which is absent in the DNN model. The used perturbation amplitudes of [30, 20, 20, 10, 10, 5, 5] mV and frequencies of [80, 200, 120, 360, 520, 760, 920] Hz used are also used in the remainder of the paper.

Realizing Boolean logic functionality by gradient descent *in materio*

Finally, we apply gradient descent *in materio* in combination with HGE to realize Boolean logic; see Fig. 4. Boolean logic, and in particular realization of the X(N)OR gate, is a valuable benchmark task that we previously used to demonstrate the ability of our DNPU to perform nonlinear classification^{15,16}. Input terminals 2 and 3 are used as data input terminals. The remaining input voltages are used as control parameters to be optimized and are tuned as explained in Fig. 1. Other choices of input and control terminals would yield comparable results¹⁶. The output current in response to the two time-dependent input signals given in Fig. 4a is first measured and then separated into the four logical input combinations (00,01,10,11). For each case, the gradient with respect to the control voltages is extracted using HGE *in materio*. The extracted gradients for the four input combinations are then summed to perform a (batch) gradient descent step (see Methods for the update scheme).

The loss function used for the optimization of a specific Boolean functionality is a combination of a correlation and a sigmoid function, promoting both the specific desired form and separation of the output currents for the four different input combinations¹⁶. As shown in Fig. 4b, all Boolean logic gates are found (red curves). The ‘true’ and ‘false’ cases can be separated by defining a threshold current as decision boundary.

Examples of such decision boundaries are indicated by the dashed lines, which could be automatically determined by training a single perceptron on the output and target data.

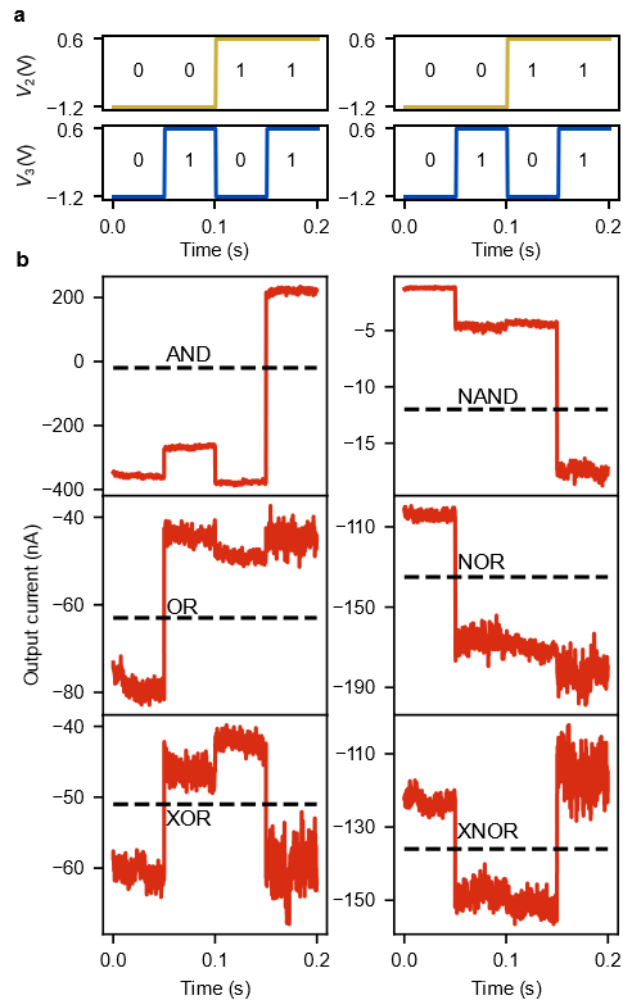


Figure 4 | Gradient descent *in materio* for realizing Boolean logic. **a**, Input signals for the realization of logic gates. Terminals 2 and 3 are used for input voltages, while the remaining terminal voltages are optimized using gradient descent *in materio*. The input values '0' and '1' are represented by -1.2 V and 0.6 V, respectively **b**, Output currents of the optimized Boolean logic gates. The horizontal dashed lines indicate an output decision boundary that could be used for separation of logical outputs '0' and '1'. For clarity, the output signal is processed such that the ramping up and down between the different data inputs (corresponding to 20 ms ramping time) is removed from this figure.

Discussion

We have proposed a generally applicable homodyne gradient extraction (HGE) method to obtain the gradient of the output response with respect to the input signals of complex nanoelectronic devices. The approach was demonstrated *in materio* for complex dopant networks in silicon. Our approach is general and

can also be applied to other physical devices and systems, including quantum dot devices^{36,37}, integrated optical systems, and metasurfaces³⁸, as long as one can establish the output response with respect to perturbations in the input signals. The key feature of the approach is the simultaneous sinusoidal perturbation of the control signals with different frequencies. Owing to the orthogonality of sinusoidal functions, the derivatives of the output response with respect to all the input signals can be extracted simultaneously by a homodyne lock-in-type technique. We demonstrated this for a device with 7 inputs and 1 output, but our approach is applicable to any number of inputs and outputs. Once the gradient information of the device is known, any first-order, gradient-based optimization scheme can be used to tune the control parameters to a desired functionality of the device by gradient descent *in materio*. We demonstrated how the approach can be utilized to obtain Boolean functionality in dopant network devices. In the present work, we still implemented the gradient extraction on an external computer. However, since the implementation only requires simple arithmetic operations and a small memory allocation per input terminal, it is straightforward to realize embedded solutions of our approach without need for external computing. We foresee that our approach will facilitate *material-based edge learning*, *i.e.* material-based systems for artificial intelligence that are independent of a centralized training procedure and that can continuously integrate data in a changing environment. Thus, applications of our method are envisioned for online-learning scenarios in edge computing, autonomous adaptive control and deep reinforcement learning systems where sensory information is directly processed by material-based computing.

Methods

Samples

The samples used in this study consist of a p-type silicon substrate (resistivity 1-20 Ω cm) doped with arsenic donors. The device fabrication was detailed in our previous work, Ref. 34.

Measurement setup

During all measurements the devices were inserted into a liquid-nitrogen (77 K) dewar with a customized dipstick. The input voltages are supplied by a National Instruments cDAQ 9264, with a -2V to 2V voltage range. The I/V converter for the output current was placed on the printed circuit board (PCB) of the device to avoid capacitive crosstalk in the wiring between the dipped device and the output sampler. The output is sampled by a National Instruments cDAQ 9202, which has a maximum sample rate of 10,000 Hz. Therefore, the sample rate of the cDAQ 9264 was also set to 10,000 Hz.

Update scheme

An iterative scheme is used to update the control voltages to be optimized, given by

$$\mathbf{V}^{(n+1)} = \mathbf{V}^{(n)} - \eta \nabla E(\mathbf{V}^{(n)}),$$

where \mathbf{V} is the vector of control voltages, E is the loss function (see Methods: Loss function) and η is the learning rate, which is set to 0.02. The optimization ran for 100 iterations or was halted earlier when E reached a threshold value, which was set to 0.3 for XOR and XNOR, and 0.15 for the other logic gates. The gradient with respect to the control voltages is split into two parts using the chain rule:

$$\nabla E(\mathbf{V}) = \frac{dE}{dI_{\text{out}}} \nabla I(\mathbf{V}),$$

where I_{out} is the output current. The first term is straightforward to calculate since we have an analytical expression of the loss function. The second term is determined using homodyne gradient extraction (HGE). See Methods: Homodyne gradient extraction (HGE) for details.

Homodyne gradient extraction (HGE)

Our homodyne gradient extraction (HGE) approach extracts the derivatives (gradient components) with respect to each input voltage simultaneously by perturbing each input voltage with sinusoidal perturbation of a distinct frequency. Our nanoelectronic device can be described by a function I which returns the output current for the N input voltages: $I(V_1, V_2, \dots, V_N) = I_{\text{out}}$. We perturb each input voltage sinusoidally with a

distinct frequency f_n and, for generality, a distinct amplitude α_n . We assume that the perturbations are small enough such that a first-order Taylor expansion of I in the input voltages is valid. The resulting outcome is:

$$\begin{aligned}
& I(V_1 + \alpha_1 \sin(2\pi f_1 t + \phi_1), V_2 + \alpha_2 \sin(2\pi f_2 t + \phi_2), \dots, V_N + \alpha_N \sin(2\pi f_N t + \phi_N)) \\
& \approx I(V_1, V_2, \dots, V_N) + \frac{\partial I}{\partial V_1} \alpha_1 \sin(2\pi f_1 t + \phi_1) + \frac{\partial I}{\partial V_2} \alpha_2 \sin(2\pi f_2 t + \phi_2) + \dots + \frac{\partial I}{\partial V_N} \alpha_N \sin(2\pi f_N t + \phi_N) \\
& \equiv I_{\text{out}} + I_1 \sin(2\pi f_1 t + \phi_1) + I_2 \sin(2\pi f_2 t + \phi_2) + \dots + I_N \sin(2\pi f_N t + \phi_N) \\
& = I_{\text{out}} + \sum_{n=1}^N I_n \sin(2\pi f_n t + \phi_n), \tag{1}
\end{aligned}$$

where I_n and ϕ_n are the amplitude and phase, respectively, of the sinusoidal modulation of the output current resulting from perturbing voltage n .

As clear from the expression above, the amplitude of the n^{th} sinusoidal modulation of the output current is proportional to the n^{th} partial derivative, and hence the n^{th} component of the gradient $\nabla I(\mathbf{V})$. By making use of the orthogonality of sine waves, we can extract the gradient information of each component separately. This homodyne procedure is similar to what is done in lock-in amplifiers. The measured output signal is first filtered to remove its DC component and then multiplied with a reference signal (currently done in software). This reference signal consists of a sine wave with frequency f_m of the perturbation on the electrode m for which we want to determine the derivative. This results in

$$\begin{aligned}
& \sum_{n=1}^N I_n \sin(2\pi f_n t + \phi_n) \sin(f_m t) \\
& = \sum_{n=1}^N \frac{I_n}{2} [\cos(2\pi(f_m - f_n)t + \phi_n) - \cos(2\pi(f_m + f_n)t + \phi_n)]. \tag{2}
\end{aligned}$$

Next, just as done in a lock-in amplifier, the resulting signal is averaged over time to remove undesired components coming from frequencies other than f_m . Since sine waves with different frequencies are orthogonal in the space of all time-dependent functions (meaning that their inner product is zero), any component with frequency unequal to f_m is attenuated to zero for long enough averaging time T (much longer than the period of the lowest frequency). We thus obtain after averaging

$$I_{\text{average}} \approx \frac{I_m}{2} \cos(\phi_m). \quad (3)$$

This expression still depends on the phase ϕ_m . To extract this phase, the output signal is multiplied with a sine wave with a frequency f_m , but a phase shifted over 90 degrees. As a result, two signals are obtained: an *in-phase* signal $X = \frac{I_m}{2} \cos(\phi_m)$ and a *quadrature* signal $Y = \frac{I_m}{2} \sin(\phi_m)$. The amplitude is then determined as $I_m = 2\sqrt{X^2 + Y^2}$ and the phase as $\phi_m = \arctan\left(\frac{Y}{X}\right)$.

Since the perturbation applied to each input terminal has a distinct frequency, we can calculate the values I_m for all terminals m simultaneously from a single measurement of the output signal by repeating the above procedure for each frequency f_m . The final step in obtaining the derivatives with respect to each input voltage is dividing the values I_m by the amplitudes of the perturbations α_m . The derivatives are then given by $\frac{\partial I}{\partial V_m} = \rho_m \frac{I_m}{\alpha_m}$, where ρ_m is the sign of the gradient, with values 1 or -1 for $\phi_m \in [-90, 90]$ or $\phi_m \in [90, 270]$ degrees, respectively.

To ensure an accurate extraction of the gradient, the following issues must be taken into consideration. First, undesired contributions to I_{average} attenuate to zero only for long averaging times T . It is therefore crucial to take T sufficiently large. Second, the frequencies f_n should ideally be chosen in a low-noise frequency domain because otherwise the above procedure will pick up spurious noise contributions. Because of the presence of $1/f$ noise³⁴ higher perturbation frequencies will in principle yield more accurate results. On the other hand, the perturbation frequencies should be sufficiently low to be in the static response regime of the device. Next, the sampling frequencies of the input and output signals should be high enough to avoid numerical errors in the integration of the product of the output signal and the reference signal. The sum of the highest two chosen perturbation frequencies can be used to decide upon sampling frequency, due to the term with frequency $(f_m + f_n)$ in Eq. (2). Finally, the magnitude α_n of the perturbations should be low enough to be in the linear response regime of the device. For too large perturbations, the response of the device will no longer be given by Eq. (1), but will contain non-linear contributions with sum and difference frequencies of

the perturbation frequencies. This also means that the perturbation frequencies should preferably be chosen such that their sums and differences are not too close to these frequencies themselves.

HGE in the DNN model

To allow a comparison to the physical measurements, we choose the HGE parameters for the DNN model such that they closely match with those used for the real device. Since the sample rate of the input and output modules connected to the real device were set to 10,000 Hz (see Methods: Measurement setup) and the signals were applied for 0.125 s, we used $10,000 \times 0.125$ datapoints in the DNN model. The frequencies and amplitudes of the sinusoidal perturbations are [80, 200, 120, 270, 520, 760, 920] Hz and [30, 20, 20, 10, 10, 5, 5] mV for V_1 to V_7 , respectively. The input signals are applied for 10 oscillation periods of the lowest perturbation frequency, *i.e.* 800 datapoints, which corresponds to 0.125 s in the physical device. The range of the inputs is -1 to +1 V. Note that the inputs and outputs DNN model are actually unitless, but are trained to represent values in Volts and Ampere. We random-uniformly sampled 3,000 points from the specified input range and computed the gradient with both the backpropagation method and the HGE method.

Loss function

The loss function to obtain Boolean logic functionality (the same as used in Ref. 16) is given by $E(y, z) = (1 - \rho(y, z)) / \sigma(y_{\text{sep}})$, where y are the measured currents, z the targeted currents, $\rho(y, z)$ is the Pearson correlation coefficient and σ the sigmoid function. The value y_{sep} represents the minimum separation between the high and low labelled data. For the data labelled as logic ‘1’ (or high output) the lowest predicted current is taken and for the data labelled as logic ‘0’ (or low output) the highest predicted current is taken, which are subtracted to obtain y_{sep} . While the correlation function promotes similarity between the targeted and predicted outputs, the sigmoid function promotes separation between the two logic current levels.

In the Extended Data Fig. 4 the results for Boolean logic gates in the Si:B device are given. To demonstrate that gradient descent *in materio* is not restricted to a particular loss function, these solutions are found with a mean squared error (MSE), which is given by $E(y, z) = \frac{1}{N} \sum_{i=1}^N (y_i - z_i)^2$. The MSE is a well-

known loss function and has the advantage that the gradient of this function can be easily incorporated in electronics, allowing the creation of fully autonomous systems. A disadvantage is that the target values are set to a fixed output, which strongly limits the solution space.

Data availability: The data presented here are available from the corresponding author on reasonable request.

Code availability: The custom computer code used here is available under the GNU General Public License v3.0 at <https://github.com/BraiNEdarwin/brains-py>

References

1. LeCun, Y., Bengio, Y. & Hinton, G. Deep learning. *Nature* **521**, 436–444 (2015).
2. Rumelhart, D. E., Hinton, G. E. & Williams, R. J. *Learning Internal Representations by Error Propagation*. <https://apps.dtic.mil/docs/citations/ADA164453> (1985).
3. Werbos, P. Beyond Regression : *Ph Diss. Harv. Univ.* (1974).
4. Lecun, Y., Bottou, L., Bengio, Y. & Haffner, P. Gradient-based learning applied to document recognition. *Proc. IEEE* **86**, 2278–2324 (1998).
5. Strubell, E., Ganesh, A. & McCallum, A. Energy and Policy Considerations for Modern Deep Learning Research. *Proc. AAAI Conf. Artif. Intell.* **34**, 13693–13696 (2020).
6. Akopyan, F. *et al.* TrueNorth: Design and Tool Flow of a 65 mW 1 Million Neuron Programmable Neurosynaptic Chip. *IEEE Trans. Comput.-Aided Des. Integr. Circuits Syst.* **34**, 1537–1557 (2015).
7. Davies, M. *et al.* Loihi: A Neuromorphic Manycore Processor with On-Chip Learning. *IEEE Micro* **38**, 82–99 (2018).
8. Jouppi, N. P. *et al.* In-Datcenter Performance Analysis of a Tensor Processing Unit. in *Proceedings of the 44th Annual International Symposium on Computer Architecture* 1–12 (Association for Computing Machinery, 2017). doi:10.1145/3079856.3080246.
9. Feldmann, J. *et al.* Parallel convolutional processing using an integrated photonic tensor core. *Nature* **589**, 52–58 (2021).

10. McMahon, P. L. *et al.* A fully programmable 100-spin coherent Ising machine with all-to-all connections. *Science* **354**, 614–617 (2016).
11. Grollier, J., Querlioz, D. & Stiles, M. D. Spintronic Nanodevices for Bioinspired Computing. *Proc. IEEE* **104**, 2024–2039 (2016).
12. Romera, M. *et al.* Vowel recognition with four coupled spin-torque nano-oscillators. *Nature* **563**, 230–234 (2018).
13. Kaspar, C., Ravoo, B. J., van der Wiel, W. G., Wegner, S. V. & Pernice, W. H. P. The Rise of Intelligent Matter. *Nature* (2021).
14. Bose, S. K., Lawrence, C. P. *et al.* Evolution of a designless nanoparticle network into reconfigurable Boolean logic. *Nat. Nanotechnol.* **10**, 1048–1052 (2015).
15. Chen, T. *et al.* Classification with a disordered dopant atom network in silicon. *Nature* **577**, 341–345 (2020).
16. Ruiz Euler, H.-C., Boon, M. N. *et al.* A deep-learning approach to realizing functionality in nanoelectronic devices. *Nat. Nanotechnol.* **15**, 992–998 (2020).
17. van Diepen, C. J. *et al.* Automated tuning of inter-dot tunnel coupling in double quantum dots. *Appl. Phys. Lett.* **113**, 033101 (2018).
18. Botzem, T. *et al.* Tuning Methods for Semiconductor Spin Qubits. *Phys. Rev. Appl.* **10**, 054026 (2018).
19. Baart, T. A., Eendebak, P. T., Reichl, C., Wegscheider, W. & Vandersypen, L. M. K. Computer-automated tuning of semiconductor double quantum dots into the single-electron regime. *Appl. Phys. Lett.* **108**, 213104 (2016).
20. Lapointe-Major, M. *et al.* Algorithm for automated tuning of a quantum dot into the single-electron regime. *Phys. Rev. B* **102**, 085301 (2020).
21. Zwolak, J. P. *et al.* Autotuning of Double-Dot Devices In Situ with Machine Learning. *Phys. Rev. Appl.* **13**, 034075 (2020).
22. Durrer, R. *et al.* Automated Tuning of Double Quantum Dots into Specific Charge States Using Neural Networks. *Phys. Rev. Appl.* **13**, 054019 (2020).

23. Darulová, J. *et al.* Autonomous Tuning and Charge-State Detection of Gate-Defined Quantum Dots. *Phys. Rev. Appl.* **13**, 054005 (2020).
24. Lennon, D. T. *et al.* Efficiently measuring a quantum device using machine learning. *Npj Quantum Inf.* **5**, 1–8 (2019).
25. Teske, J. D. *et al.* A machine learning approach for automated fine-tuning of semiconductor spin qubits. *Appl. Phys. Lett.* **114**, 133102 (2019).
26. Torrejon, J. *et al.* Neuromorphic computing with nanoscale spintronic oscillators. *Nature* **547**, 428–431 (2017).
27. Strukov, D. B., Snider, G. S., Stewart, D. R. & Williams, R. S. The missing memristor found. *Nature* **453**, 80–83 (2008).
28. Stepney, S. The neglected pillar of material computation. *Phys. Nonlinear Phenom.* **237**, 1157–1164 (2008).
29. Miller, J. F. & Downing, K. Evolution in materio: looking beyond the silicon box. in *Proceedings 2002 NASA/DoD Conference on Evolvable Hardware* 167–176 (2002). doi:10.1109/EH.2002.1029882.
30. Kiraly, B., Knol, E. J., van Weerdenburg, W. M. J., Kappen, H. J. & Khajetoorians, A. A. An atomic Boltzmann machine capable of self-adaption. *Nat. Nanotechnol.* 1–7 (2021) doi:10.1038/s41565-020-00838-4.
31. Jabri, M. & Flower, B. Weight Perturbation: An Optimal Architecture and Learning Technique for Analog VLSI Feedforward and Recurrent Multilayer Networks. *IEEE Trans. Neural Netw. Publ. IEEE Neural Netw. Counc.* **3**, 154–7 (1992).
32. Spall, J. C. Multivariate stochastic approximation using a simultaneous perturbation gradient approximation. *IEEE Trans. Autom. Control* **37**, 332–341 (1992).
33. Alspector, J., Meir, R., Yuhas, B., Jayakumar, A. & Lippe, D. A parallel gradient descent method for learning in analog VLSI neural networks. in *Proceedings of the 5th International Conference on Neural Information Processing Systems* 836–844 (Morgan Kaufmann Publishers Inc., 1992).
34. Chen, T., Bobbert, P. A. & Wiel, W. G. van der. 1/f Noise and Machine Intelligence in a Nonlinear Dopant Atom Network. *Small Sci.* 2000014 (2021) doi:https://doi.org/10.1002/smssc.202000014.

35. Cover, T. M. Geometrical and Statistical Properties of Systems of Linear Inequalities with Applications in Pattern Recognition. *IEEE Trans. Electron. Comput.* **EC-14**, 326–334 (1965).
36. Li, R. *et al.* A crossbar network for silicon quantum dot qubits. *Sci. Adv.* **4**, eaar3960 (2018).
37. Veldhorst, M., Eenink, H. G. J., Yang, C. H. & Dzurak, A. S. Silicon CMOS architecture for a spin-based quantum computer. *Nat. Commun.* **8**, 1–8 (2017).
38. Tsilipakos, O. *et al.* Toward Intelligent Metasurfaces: The Progress from Globally Tunable Metasurfaces to Software-Defined Metasurfaces with an Embedded Network of Controllers. *Adv. Opt. Mater.* **8**, 2000783 (2020).

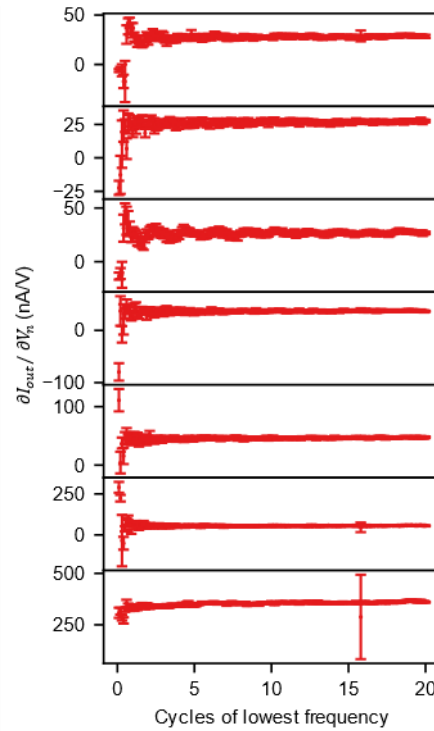
Acknowledgments: We thank B. J. Geurts and H. Broersma for fruitful discussions. We thank M. H. Siekman and J. G. M. Sanderink for technical support. We acknowledge financial support from the University of Twente, the Dutch Research Council (Natuurkunde Projectruimte grant no. 680-91-114 and HTSM grant no. 16237) and Toyota Motor Europe N.V.

Author contributions: M.N.B. performed the measurements. H.-C.R.E. performed the simulations. M.N.B. and T.C. designed the experiments. B.v.d.V. and T.C. fabricated the samples. U.A.I. helped to develop the general software framework. M.N.B, H.-C.R.E and W.G.v.d.W. wrote the manuscript. T.C., H.-C.R.E. and W.G.v.d.W. conceived the project. W.G.v.d.W. and P.A.B. supervised the project.

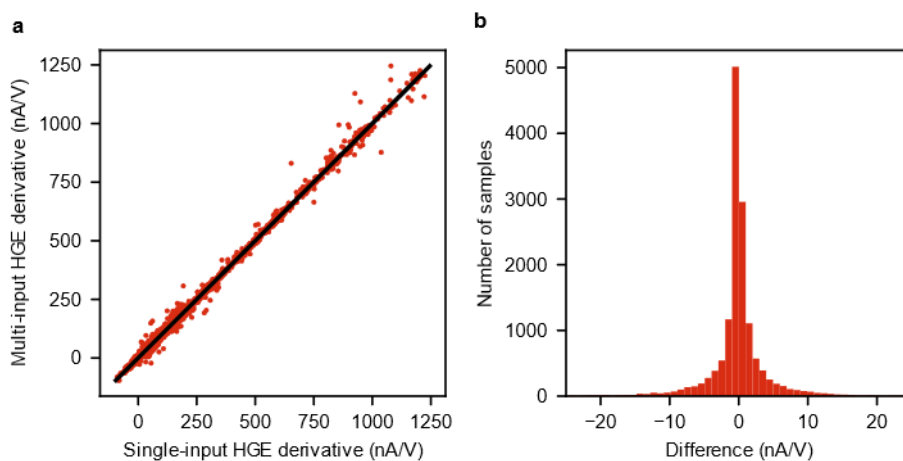
Competing interests: The authors declare no competing interests.

Materials & Correspondence: Correspondence and requests of material should be addressed to W.G.v.d.W. (W.G.vanderWiel@utwente.nl).

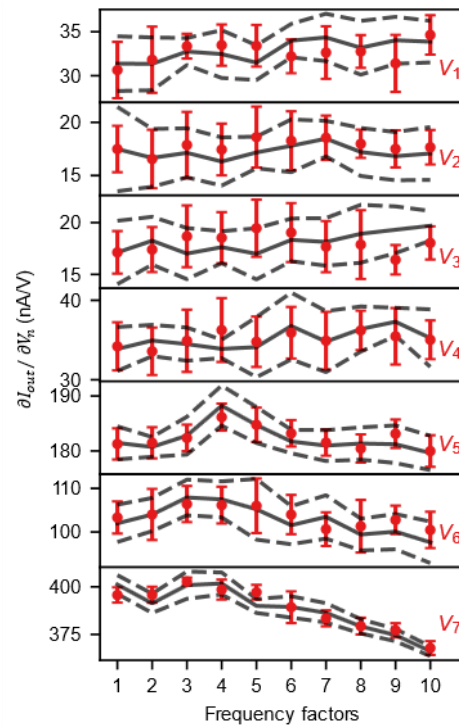
Extended Data



Extended Data Figure 1 | Convergence of homodyne gradient extraction (HGE) gradient for increasing sample times in a Si:B device. The accuracy of the gradient estimation increases with sampling time. The input terminals 1 to 7 are biased with a random DC voltage $[-0.936, -0.424, -0.352, -0.947, -0.375, -0.351, -0.470]$ V and perturbation frequencies $[6, 15, 9, 27, 39, 57, 69]$ Hz and amplitudes $[30, 20, 20, 10, 10, 5, 5]$ mV. The error bars represent the standard deviation of 10 measurements.

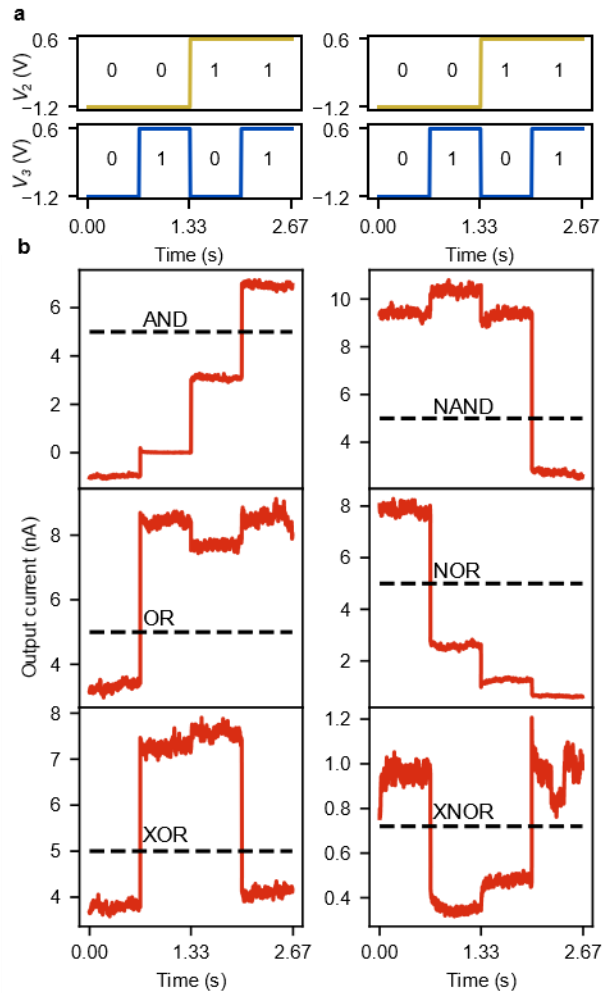


Extended Data Figure 2 | Accuracy analysis of HGE derivatives in a Si:B device. a, Comparison between the single- and multi-input HGE derivatives for 1,850 random input voltages in the range $[-1.2, 0.6]$ V. The perturbation frequencies and amplitudes are $[6, 15, 9, 27, 39, 57, 69]$ Hz and $[30, 20, 20, 10, 10, 5, 5]$ mV for (V_1, V_7) , respectively. The solid line has unity slope. **b,** Histogram of the difference in the single- and multi-input HGE derivatives for the data shown in a, showing that the error is symmetrically centred around 0.

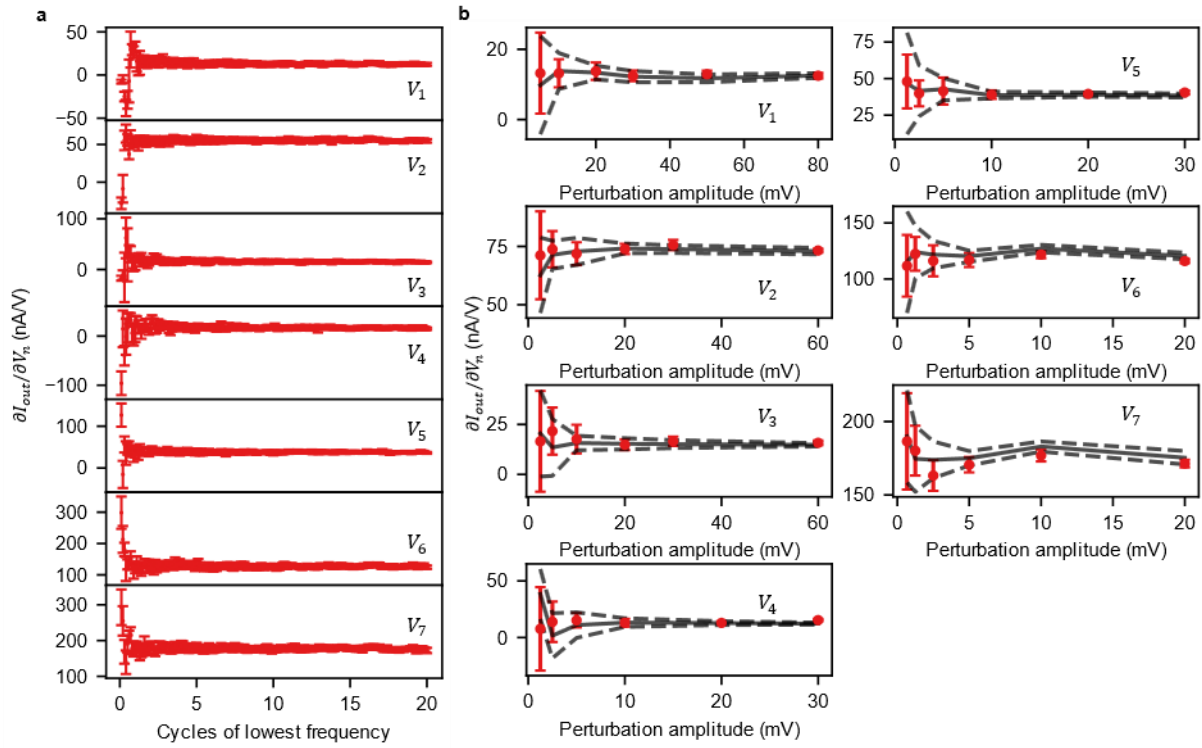


Extended Data Figure 3 | Comparison of single- and multi-input HGE derivatives for increasing frequencies in a Si:B device.

A random DC input voltage is applied to all input terminals ($[-0.152, -0.844, -1.067, -0.428, 0.011, -0.711, -0.572]$ V for (V_1, V_7)). Additionally, perturbations are added to input terminals 1 to 7, having distinct amplitudes and base frequencies of [30, 20, 20, 10, 10, 5, 5] mV and [2, 5, 3, 9, 13, 19, 23] Hz, respectively. The derivatives of this experiment with respect to electrode 1 to 7 are represented by the coloured data points and are labelled as V_1 to V_7 . The black solid curves correspond to single-input HGE measurements, where all input terminals have the same DC voltage, but only one terminal is perturbed. The error bars and dashed curves represent the standard deviations of 10 measurements of the multi- and single-input HGE derivatives, respectively. The experiment is repeated for multiple magnitudes of the base frequencies, given by the ‘frequency factor’, which is a multiplication factor to the base frequencies.



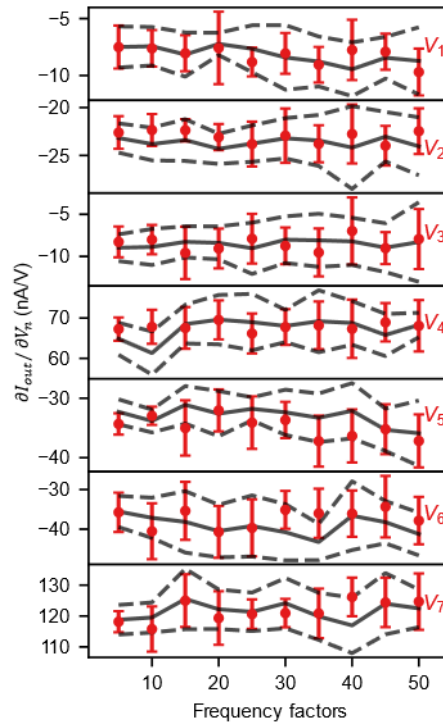
Extended Data Figure 4 | Gradient descent *in materio* for realizing Boolean logic in a Si:B device. **a**, Input signals for the realization of logic gates. Terminals 2 and 3 are used as input voltages, while the remaining voltages are optimized using the proposed gradient descent method. The input values ‘0’ and ‘1’ are represented by -1.2 V and 0.6 V, respectively **b**, Output currents of the optimized Boolean logic gates with a normalized mean squared error loss function. The target currents are set to 0 and 10 for the inputs ‘0’ and ‘1’ for all logic gates, except for XNOR, which had target current of 1 for input ‘1’. The horizontal dashed lines indicate an output decision boundary that could be used for separation of logical outputs ‘0’ and ‘1’. For clarity, the output signal is processed such that the ramping up and down between the different data inputs (corresponding to 20 ms ramping time) is removed from this figure.



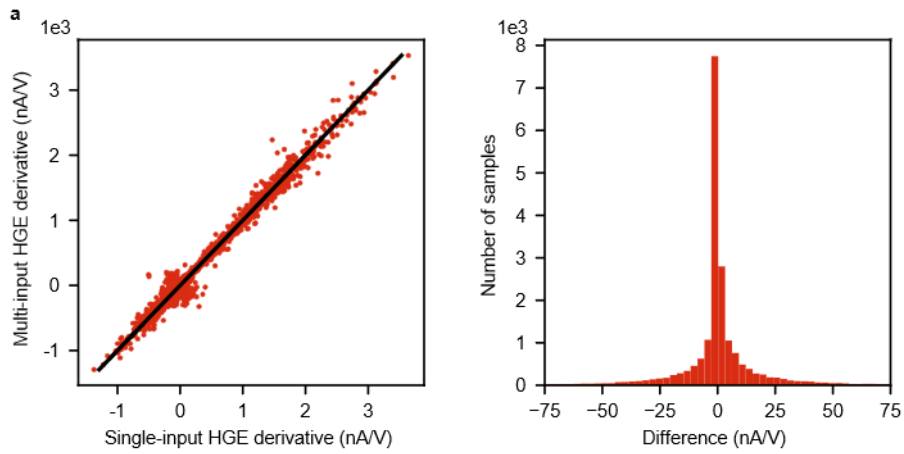
Extended Data Figure 5 | HGE analysis for all input terminals. **a**, Multi-input HGE derivatives as a function of time. The inputs 1 - 7 are biased with a random DC voltage ([1.071, -0.107, 0.278, 0.285, 0.828, 0.282, 0.443] V for terminals 1 - 7) and sinusoidal perturbations with frequencies [20, 50, 30, 90, 130, 190, 230] Hz and amplitudes [30, 20, 20, 10, 10, 5, 5] mV. The longest sampling time is 1 second, corresponding to 20 oscillation cycles of the lowest frequency. **b**, Extracted derivatives as function of perturbation amplitude. The same DC voltages are used as in **a**. The amplitude of the perturbations are given in Extended Data Table 1. Symbols with error bars: multi-input HGE with 0.5 s measurement time (10 cycles of lowest frequency). Full lines with errors given by dashed lines: single-input HGE with 0.5 s measurement time. The errors represent standard deviations of 10 measurements.

Extended Data Table 1 | Perturbation amplitudes for the convergence results shown in Fig. 2 d, e.

Terminal	1	2	3	4	5	6	7
Amplitude 1 (mV)	5	2.5	2.5	1.25	1.25	0.675	0.675
Amplitude 2 (mV)	10	5	5	2.5	2.5	1.25	1.25
Amplitude 3 (mV)	20	10	10	5	5	2.5	2.5
Amplitude 4 (mV)	30	20	20	10	10	5	5
Amplitude 5 (mV)	50	30	30	20	20	10	10
Amplitude 6 (mV)	80	60	60	30	30	20	20



Extended Data Figure 6 | Comparison of single- and multi-input HGE derivatives for increasing frequencies. A random DC input voltage is applied to all input terminals ([-1.081, -0.290, -0.854, -1.129, -0.455, -0.526, -0.967] V for terminals 1 to 7, respectively). Additionally, perturbations are added to input terminals 1 to 7, having distinct amplitudes and base frequencies of [30, 20, 20, 10, 10, 5, 5] mV and [2, 5, 3, 9, 13, 19, 23] Hz, respectively. The derivatives of this experiment with respect to electrode 1 to 7 are represented by the coloured data points and are labelled as V_1 to V_7 . The black solid curves correspond to single-input HGE measurements, where all input terminals have the same DC voltage, but only one terminal is perturbed. The error bars and dashed curves represent the standard deviations of 10 measurements of the multi- and single-input HGE derivatives, respectively. The experiment is repeated for multiple magnitudes of the base frequencies, given by the ‘frequency factor’, which is a multiplication factor to the base frequencies.



Extended Data Figure 7 | Accuracy analysis of HGE derivatives for alternative frequencies. a, Comparison between the single- and multi-input HGE derivatives for 2,528 random input voltages in the range $[-1.2, 0.6]$ V. The perturbation frequencies and amplitudes are $[80, 160, 240, 320, 400, 480, 560]$ Hz and $[30, 20, 20, 10, 10, 5, 5]$ mV for (V_1, V_7) , respectively. Thus, the picked frequencies are harmonics of the lowest frequency. Nonetheless, the single-input and multi-input HGE derivatives are similar. The solid line has unity slope. **b,** Histogram of the difference in the single- and multi-input HGE derivatives for the data shown in a, showing that the error is symmetrically centred around 0.

Supplementary Information

Supplementary Notes

1. Si:B experiments

The measurements for the Si:B device are conducted in a different measurement setup, where the bandwidth of the setup is only 100 Hz. Therefore, the perturbation frequencies used in these experiments are lower than in the main text. The fabrication procedure of the Si:B sample is described in Ref. 15. The results are shown in Extended Data Fig. 1 - 4.

2. HGE for increasing frequency

To demonstrate that HGE is insensitive of the magnitude of the frequencies, we take a single set of input voltages and extract the gradient as a function of frequency. For this experiment we take as base frequencies [2, 5, 3, 9, 13, 19, 23] Hz and multiply these frequencies with factors of increasing magnitude, which is referred to as the ‘frequency factor’. The resulting derivatives are shown in Extended Data Figure 6, where the coloured data represent the multi-input HGE derivatives, and the black solid lines represent the single-input HGE derivatives. The error bars and the dashed lines represent the standard deviations of 10 measurements. Note that the input and output sampling frequency was limited to 10 kHz. The highest input frequency used (at a frequency factor of 50) is $50 \times 23 = 1,150$ Hz, meaning that the input (and output) signal consists of only 8 to 9 points per wavelength. Nevertheless, the HGE gradient for this frequency factor seems not to have degraded compared to the lower frequency factors that have more points per wavelength.